

AFRL-AFOSR-UK-TR-2015-0042



Advanced Photonic Hybrid Materials

Stephane Parola

**UNIVERSITE LYON 1 CLAUDE BERNARD
43 BOULEVARD DU 11 NOVEMBRE 1918
VILLEURBANNE, 69100
FRANCE**

EOARD Grant #FA8655-12-1-2106

Report Date: July 2015

Final Report from 29 May 2012 to 27 May 2015

Distribution Statement A: Approved for public release distribution is unlimited.

**Air Force Research Laboratory
Air Force Office of Scientific Research
European Office of Aerospace Research and Development
Unit 4515, APO AE 09421-4515**

REPORT DOCUMENTATION PAGE					<i>Form Approved</i> OMB No. 0704-0188	
<p>The public reporting burden for this collection of information is estimated to average 1 hour per response, including the time for reviewing instructions, searching existing data sources, gathering and maintaining the data needed, and completing and reviewing the collection of information. Send comments regarding this burden estimate or any other aspect of this collection of information, including suggestions for reducing the burden, to Department of Defense, Washington Headquarters Services, Directorate for Information Operations and Reports (0704-0188), 1215 Jefferson Davis Highway, Suite 1204, Arlington, VA 22202-4302. Respondents should be aware that notwithstanding any other provision of law, no person shall be subject to any penalty for failing to comply with a collection of information if it does not display a currently valid OMB control number.</p> <p>PLEASE DO NOT RETURN YOUR FORM TO THE ABOVE ADDRESS.</p>						
1. REPORT DATE (DD-MM-YYYY) 07/22/2015		2. REPORT TYPE Final			3. DATES COVERED (From - To) 29 May 2012 - 27 May 2015	
4. TITLE AND SUBTITLE Advanced Photonic Hybrid Materials				5a. CONTRACT NUMBER		
				5b. GRANT NUMBER FA8655-12-1-2106		
				5c. PROGRAM ELEMENT NUMBER 61102F		
6. AUTHOR(S) Stephane Parola				5d. PROJECT NUMBER		
				5e. TASK NUMBER		
				5f. WORK UNIT NUMBER		
7. PERFORMING ORGANIZATION NAME(S) AND ADDRESS(ES) UNIVERSITE LYON 1 CLAUDE BERNARD 43 BOULEVARD DU 11 NOVEMBRE 1918 VILLEURBANNE, 69100 FRANCE					8. PERFORMING ORGANIZATION REPORT NUMBER N/A	
9. SPONSORING/MONITORING AGENCY NAME(S) AND ADDRESS(ES) EOARD Unit 4515 APO AE 09421-4515					10. SPONSOR/MONITOR'S ACRONYM(S) AFRL/AFOSR/IOE (EOARD)	
					11. SPONSOR/MONITOR'S REPORT NUMBER(S) AFRL-AFOSR-UK-TR-2015-0042	
12. DISTRIBUTION/AVAILABILITY STATEMENT Distribution A: Approved for public release; distribution is unlimited.						
13. SUPPLEMENTARY NOTES						
14. ABSTRACT This work had three results: 1) construction of gold "bipyramid" nanostructures for tuning the plasmon resonance between visible/IR wavelengths; these structures with a high aspect ratio allowed extension of the local surface plasmon resonance (LSPR) toward IR wavelengths as far as 1850nm. 2) Optical transmission properties of dispersions of self-orienting gold nanoparticles (spherical and bipyramidal) in sol-gel hybrid silica, which could be used as optical limiters (transmitting at low levels but blocking high intensities); this has been done in liquid, but this study attempted a stable solid-state glass. The transmission spectra showed well-defined plasmon absorption peaks without redshift, indicating little or no LSPR coupling.						
15. SUBJECT TERMS EOARD, nanoparticle, surface plasmon resonance, plasmon, optical limiter, luminescence						
16. SECURITY CLASSIFICATION OF:			17. LIMITATION OF ABSTRACT	18. NUMBER OF PAGES	19a. NAME OF RESPONSIBLE PERSON	
a. REPORT	b. ABSTRACT	c. THIS PAGE			PUTZ, VICTOR	
Uncl	Uncl	Uncl	SAR	23	19b. TELEPHONE NUMBER (Include area code) 011-44-1896616013	

Advanced photonic hybrid materials

Final report from S. Parola, Laboratoire de Chimie ENS Lyon, France

July 2015

PUBLICATIONS AND COMMUNICATIONS: The OARD project with reference FA8655-12-1-2106 was mentioned in all these articles and presentations.

This report is based on 3 articles (joined to the report):

- ***Dispersion and self-orientation of gold nanoparticles in sol-gel hybrid silica – optical transmission properties***, H. Lundén, A. Liotta, D. Chateau, F. Lerouge, F. Chaput, S. Parola, C. Brännlund, Z. Ghadyani, M. Kildemo, M. Lindgren, C. Lopes, J. Mater. Chem. C, 2015, 3, 1026.
- ***From gold nanobipyramids to nanojavelins for a precise tuning of the Plasmon resonance to the infrared wavelengths. Experimental and theoretical aspects***, D. Chateau, A. Liotta, F. Vadcard, J. R. G. Navarro, F. Chaput, J. Lermé, F. Lerouge, S. Parola, Nanoscale, 2015, 7, 1934.
- ***Long distance effect of plasmonic structures in hybrid sol-gel luminescent materials. Strong enhancement of optical nonlinearities in optical silica materials***, D. Chateau, A. Liotta, F. Lerouge, F. Chaput, D. Krein, T. Cooper, M. Lindgren, S. Parola, to be submitted august 2015 (collaboration AFRL).

The work was presented in several international conferences with the following references:

Invited conferences:

- Metal nanoparticles in sol-gel materials. S. Parola, NanoFuture, 3-7 february 2013, Maribor, Slovenia.
- Fluorescent hybrid gold nanoparticles, S. Parola, J. Navarro, F. Lerouge, G. Micouin, P. Baldeck, C. Monnereau, C. Andraud, A. Favier, M.-T. Charreyre, Y. Leverrier, J. Marvel, Polish-French Workshop on Organic Electronics and Nanophotonics WOREN 2013, Zlockie, Poland, Feb 2013.
- Hybrid monolithic materials with high concentrations of chromophores and metallic nanoparticles for optical protection, S. Parola, MRS 2013 Spring Meeting, San Francisco, USA, April 2013.
- Nanoparticules hybrides fluorescentes pour l'imagerie, S. Parola, GDR Imagerie, Chimie et Microscopie, Lyon, France July 2013.
- Metal nanoparticles as a tool for controlling the properties of dyes. Applications in bioimaging and optics, S. Parola, NanoApp 2013, Portoroz, Slovénie, Septembre 2013 (Keynote).
- Insights in the interactions between chromophores and metal nanoparticles for optical and bioimaging applications, S. Parola, J. Navarro, A. Liotta, D. Chateau, F. Lerouge, F. Chaput, G. Micouin, P. Baldeck, C. Monnereau, C. Andraud, XII international conference on molecular spectroscopy ICMS, From Molecules to Nano- and Biomaterials, Kraków – Białka Tatrzańska, Pologne, September 2013.
- Control of Dyes- gold nanoparticles interactions. Applications in bioimaging and optical protection. S. Parola, J. R. G. Navarro, D. Chateau, A. Liotta, F. Lerouge, F. Chaput, C. Andraud, P.L. Baldeck, Phobia Annual Nanophotonic International Conference PANIC, Wroclaw, Pologne, Avril 2014.
- Hybrid metal nanoparticles for bioimaging and optical protection, S. Parola, KOREA-FRANCE Joint Symposium, Seoul, Juin 2014.
- Nanosciences, from principles to recent developments, S. Parola, Summer school Nanoscience and Environment, Maribor, Slovénie, Juillet 2014.
- Control of interactions between dyes and gold nanoparticles. Applications in bioimaging and optical protection, S. Parola, Summer school Université Goethe Francfort / ENS Lyon, Lyon, Juillet 2014.
- Multifunctional hybrid nanoparticles for two-photon fluorescence imaging and photodynamic therapy, S. Parola, F. Vadcard, H. Rositi, F. Lerouge, M. Wiart, F. Chaput, C. Monnereau, C. Andraud, G. Micouin, N. Lascoux, P. Baldeck, A. Åslund, P. Hammarström, P. Nilsson, M. Lindgren, NABM september 2014 Iasi, Roumanie.

Oral communications:

- Efficient optical protections using dyes-nanoparticles interactions in sol-gel materials, S. Parola, D. Chateau, A. Liotta, F. Chaput, F. Lerouge, M. Lindgren, C. Lopes International Sol-Gel Conference, Madrid, Spain, September 2013.
- Controlling the interactions between gold nanoparticles and dyes for enhancement of the optical properties of hybrid materials, S. Parola, A. Liotta, J. Navarro, D. Chateau, F. Lerouge, F. Chaput, C. Andraud, G. Micouin, N. Lascoux, P. Baldeck, C. Lopes, M. Lindgren, Hybrid Materials, Sitges (Barcelona Spain), March 2015
- Composite sol-gel materials with plasmonic nanostructures for optical applications, S. Parola, F. Lerouge, D. Chateau, A. Liotta, I. Levchuk, C. Guillard, F. Chaput, D. Krein, T. Cooper, C. Lopes, M. Lindgren, International Sol-gel conference 2015, Kyoto, Japan, September 2015.

Distribution A: Approved for public release; distribution is unlimited.

TECHNICAL DESCRIPTION OF THE RESULTS:

1/ Synthesis, characterization and modelling of anisotropic gold nanoparticles (nanobipyramids) for a precise tuning of the Plasmon resonance between the visible and infrared wavelengths (see joined article for further details)

INTRODUCTION

Noble metal nanoparticles are nanoobjects exhibiting fascinating properties which are of current interest regarding the rapidly growing field of nanosciences. They can interact strongly with light and with the surrounding environment in particular due to the surface plasmon resonance. Such interaction can be used to tune the optical properties of molecular dyes located at the vicinity of the metallic surface. Furthermore, these properties are adjustable according to the metal, the shape and the size of the particles. They offer many possible applications in optics,¹⁻³ medicine,⁴⁻⁶ and catalysis.^{7,8} Enhancement of luminescence is one of the prominent research areas in connection with these applications and this is known to be mostly dependent on the distance between the dyes and the metallic surface and/or the dipole orientations.⁹⁻¹⁵ In most applications, the spectral localization of the surface plasmon resonance is also a crucial parameter in order to tune the dye-to-particle interactions due to the importance of the overlapping between the SPR and the absorption/emission bands of the chromophores on the overall optical response of the nanoobjects.¹⁶ Most of the studies concern SPR in the visible wavelength and few in the NIR, the latest are being far more difficult to achieve. The chemical composition is of course one of the parameters involved in the localization of the plasmon resonance, and we will focus on gold in this paper due to the stability and tunability of the shape of the nanoobjects.¹⁷⁻¹⁹ In the case of spherical nanoparticles, the SPR is essentially located in the visible wavelength, mostly in the range 400-600 nm. Anisotropic architectures become extremely interesting since they present several frequencies of resonance depending on the polarization (Longitudinal, transverse), the most famous example being the nanorods optical response.^{20,21} In this case, the longitudinal resonance is far more intense than the transverse one and located at higher wavelengths opening possibilities of applications in the NIR. More recently sharp structures such as nanostars and bipyramids have proven themselves to be very interesting since the field generated at their tips is very intense compared to the nanorods.²²⁻²⁴ In that context bipyramidal shapes are extremely interesting structures presenting very narrow plasmon band, typically 50 nm (at half-height) around 800 nm. The growth mechanism allowing fine control of the aspect ratio and the presence of thin tips are of great interest in regards to tuning the shape/size/truncation spectral dependence. The bipyramids were firstly obtained as biproducts and/or considered as atypical nanorods.^{25,26} Despite growing number of publications on the subject, the synthetic yields remain low and even more important the final purity is rather low since it is hard to separate bipyramids and spheres from the solution. We propose a versatile route to the synthesis of gold bipyramids (AuBP) with the possibility to have a fine-tuning on the shape, size and truncation of the nano-object and thus control precisely the longitudinal SPR band between 600 and 2000 nm.

RESULTS AND DISCUSSION

The synthesis of normal and elongated nano-bipyramids was achieved via the well known seed mediated growth approach that can be divided in two main steps : (i) synthesis of the seeds which represent a key step towards tuning of the shape, size (ii) growth of the anisotropic nanoparticles from these seeds.

Synthesis of the Bipyramids

It is first important to notice that the quality (yield, shapes) of the final AuBP strongly depends on the seeds morphology. As outlined by Guyot-sionnest, when mono crystalline seeds are used the process leads to nanorods, in the case of polycrystalline seeds bipyramids are obtained.²⁶ Usually, using seed-mediated growth processes, the seeds preparation step is the most sensitive and least reproducible one, that could involve bad reproducibility of the whole process. Synthesis parameters such as the addition speed of reducing agent (NaBH_4), the temperature of the gold salt solution during this addition and the pH of the seeds solution are fundamental. To overcome these key parameters and lower their impact, we propose an easy but critical step consisting in a quick seeds aging at 85°C. The quality of the process is thus enhanced thanks to a higher crystallinity and increased size of the final seeds (figure 1).

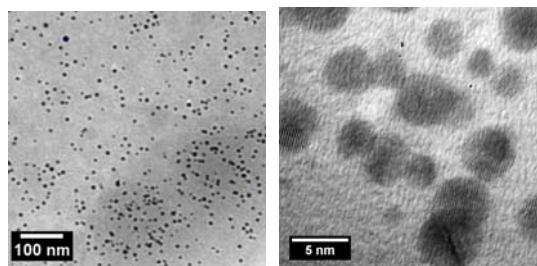


Figure 1 : TEM and HRTEM images showing polycrystallinity of the seeds after 1h aging.

The kind of surfactant used in the seeds solution is also important. It is well established that this surfactant, typically CTAB, acts as a stabilizing agent for gold nanoparticles and that the effect of the counter ion on the particle morphology is not negligible.^{27,28} Most of the time, two types of seeds are described in the literature: citrate-stabilized seeds or CTAB stabilized seeds.^{23,25,26,30}

Here we propose to use CTAC as stabilizing agent for the seeds, leading to more reactive species due to the lower affinity of CTAC for the gold surface.

The second step of the process consists in the growth of the bipyramids from the seeds by reduction of gold salt in solution in the presence of a silver salt, a reducing agent (8-Hydroxyquinoline, HQL) and surfactants. We were able to synthesize different length and shapes of bipyramids, giving us the possibility to tune their optical properties *i.e* the LSPR, in a wide range of wavelength from 600 nm to 1850 nm.

Each of the morphologies depends strongly on the kind of surfactant used during the growth process. When CTAB (Cetyltrimethylammonium bromide) was used, bipyramids featuring length in the 40 to 180 nm range were obtained (figure 2a). In the case of a mixture of CTAB and CTAC (Cetyltrimethylammonium chloride) elongated bipyramids with length in the 130 to 300 nm range were prepared (figure 2b).

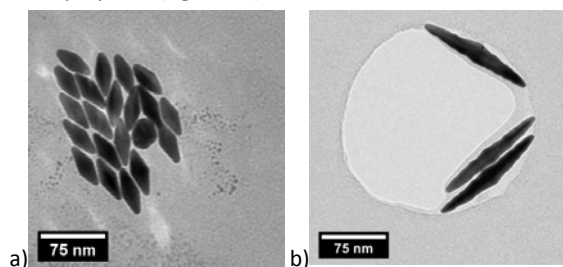


Figure 2 : Examples of bipyramids prepared with CTAB (a) and a CTAB/CTAC mixture (b)

Bipyramids prepared with CTAB show regular diamond-like shapes with straight edges. In the case of the elongated bipyramids TEM images confirmed the extremely long structures with dimensions of 15-20 nm widths and 180-250 nm length. When CTAB was used we were able to tune the size of the bipyramids by varying either the surfactant concentration or the amount of seeds added to the growth solution. Thus, a precise control of the LSPR wavelength between 500 and 1000 nm was possible. Due to the strong interactions of CTAB with the gold surface, variations in the concentration led to noticeable shifts in the LSPR although the changes were observed only for a short range of wavelength (figure 3).

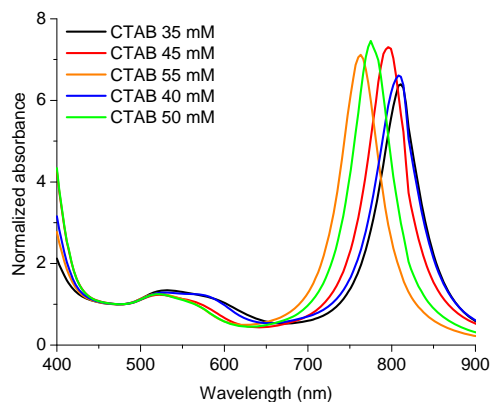


Figure 3: Absorption spectra of the bipyramids versus the surfactant concentration (normalized spectra at 480 nm). The band below 400 nm is caused by HQL impurities and degradation.

Sharp resonances in the NIR presented a shift to the blue as the CTAB concentration increased from 35 mM to 55mM. Modifying the amount of seeds at a fixed CTAB concentration (45mM) led to more remarkable results in terms of wavelength shifts (figure 4). Interestingly, when high amount of seeds where used, it was possible to grow small rice-like structures presenting a LSPR below 600nm. Although the bipyramidal structure was still observable, no sharps edges were visible. On the opposite, in the case of lower amounts, the LSPR was clearly shifted to the NIR with intense and sharp resonances in the 800 to 1000 nm range. TEM images clearly exhibited diamond like structures with sharp edges.

Although the process allows reaching high wavelengths, it is still limited in regards to the LSPR expandability towards the IR spectral ranges. This phenomenon can be attributed to the strong interaction of gold with bromide ions from CTAB, slowing down the reduction and hindering bipyramid growth by partial re-dissolution of the unstable gold tips. To overcome that issue, CTAC was used to limit bromide concentration while maintaining high surfactant concentration. Thus, by using a mixture of CTAB and CTAC, we were able to growth novel

gold nanostructures appearing as elongated bipyramids. Furthermore, by varying the CTAB/CTAC ratio it was possible to affect the length, and the LSPR, of the final objects (figure 6, 7).

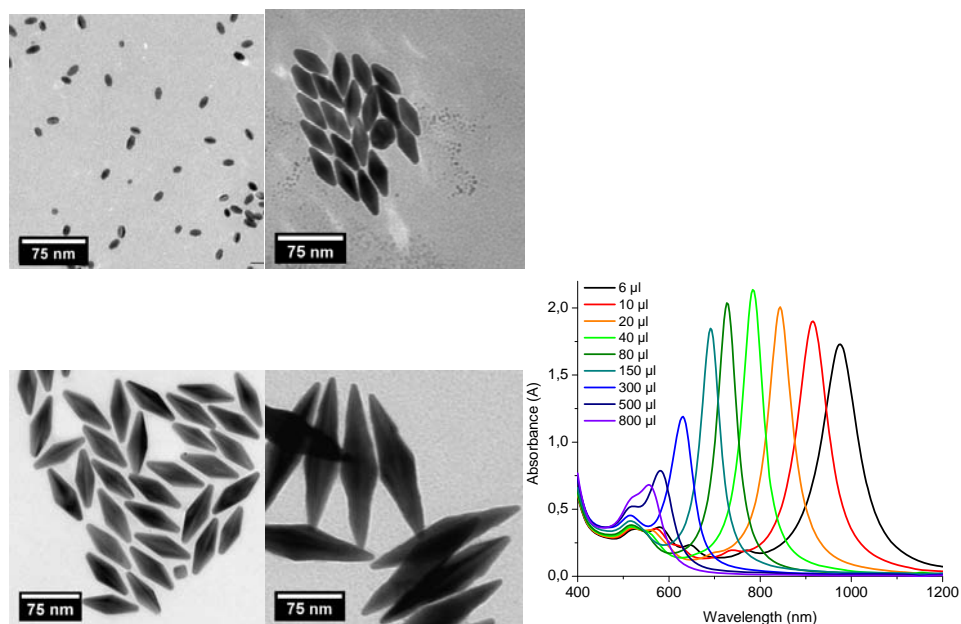


Figure 4 : TEM of bipyramids prepared with CTAB and respectively 800, 80, 40 and 6 μL of seeds suspension (left) Absorption spectra of the bipyramids versus the amount of seeds added (right). The band below 400 nm is caused by HQL impurities and degradation.

TEM pictures confirm the very high yield of this process and the only few byproducts observed are nanospheres. Whatever the CTAC/CTAB ratio, the global aspect of the structures is the same, with elongated objects exhibiting javelin-like shapes with sharp tips (estimated to 2-4 nm) and broad bases at their centre. These systems are very different from the previous ones also regarding their edges, in fact javelin like structures don't exhibit the classical diamond like profile of the previous bipyramids and the surface shows sawtooth-like structure. For a same amount of CTAC, we were able to grow elongated bipyramids with biconic shapes from 180nm for the highest quantities of CTAB, to 200 nm when CTAB was lowered.

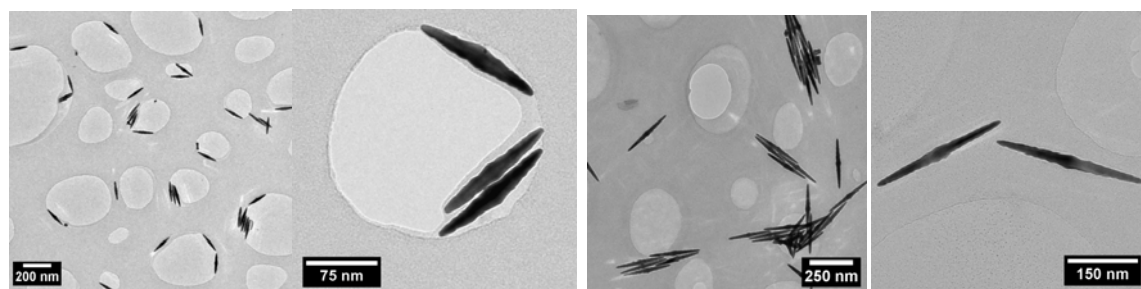


Figure 5: Elongated bipyramids (bicones) prepared with a mixture CTAB/CTAC (8 mM CTAB, 140mM CTAC, 65 μL HQL) (Top), elongated bipyramids (bicones) prepared with a mixture CTAB/CTAC (2,2 mM CTAB, 140mM CTAC, 65 μL HQL) (Bottom)

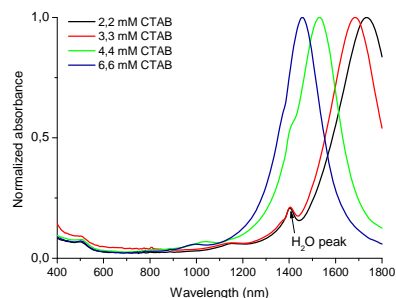


Figure 6: absorption spectra of biconic particles versus the CTAB amount (for a concentration in CTAC of 140 mM). Solution was purified by natural precipitation (1 day) of the nanoobjects provoked by increasing CTAC concentration to 180-200mM, followed by dispersion in diluted CTAC (20mM).

Bicones obtained with the CTAC/CATB mixture exhibit resonances in the 1400-1800 nm range. The band observed are very intense and sharp with a red shift observed when the amount of CTAB is lowered, which is consistent with TEM measurements. Other signals are also observed along the spectrum with smaller intensities in the 800-1200nm range probably due to quadrupolar and octupolar resonances. Finally the band exhibited at 500nm in each sample can be attributed to the larger part of the object usually assigned as their base.

The purity of the bicones was extremely high. In all cases the yield is over 80%, and in the best cases over 98%, which is unique. The sample quality was evaluated with the ratio between the AuBP LSPR peak height and the peak around 500-550nm due to the small TSPR of the bipyramids. Even though this ratio is only indicative since it is not based on the area but only on the height of the peaks, it provides information on the yield and the monodispersity of AuBP and can be seen as a signal to noise ratio of the spectra. To the best of our knowledge, even a ratio of 4 for a LSPR around 800nm for AuBP in solution has yet to be reported in the literature. The best ratios ever seen are those of Kou X. *et al.* (ratios around 3)²³ and Navarro J. *et al.* (ratios up to 3.8).²⁴ We present ratios up to 8, due to a very high yield in AuBP (up to 99%) with narrow size distribution.

The role of the reducing agent on the process was also studied (see ESI). We observed that the optical purity was much higher with HQL compared to ascorbic acid and that the surfactant concentration could be reduced more than 8 times. This can be explained by the low reductive strength of HQL which limits sphere formation. Tests conducted with other reducer, such as 2-naphtol (basically HQL without the quinoline ring) and 2-methyl-8-hydroxyquinoline proved that the quinoline ring was quite important for the purity of the nanoparticles, by slowing the reduction.

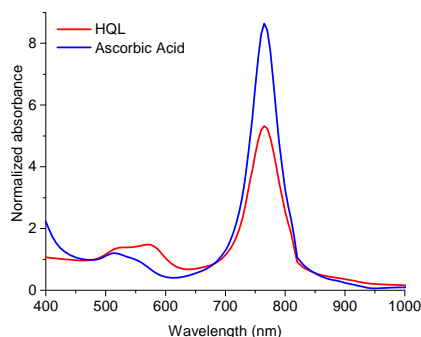


Figure xx : Comparison between 8-HQL and ascorbic acid in the synthesis. For ascorbic acid, Geitner *et Al.*³⁰ growth protocol was used since no bipyramids were obtained with our growth conditions.

The structure of both bipyramids (figure 7) and elongated particles (figure 8) was studied with SAED and HRTEM. First results show that those nanoparticles are both crystalline with a c.f.c. structure and standard lattice parameters.

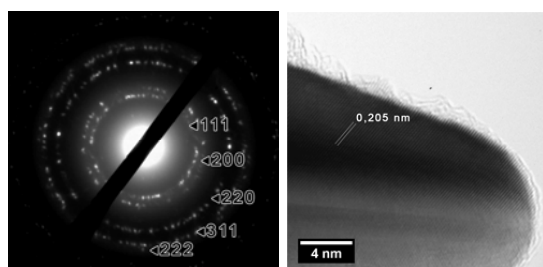


Figure 7: HRTEM, SAED pattern of a group of bipyramids (prepared in CTAB with 100 μ l of seeds suspension) and zoom on one tip.

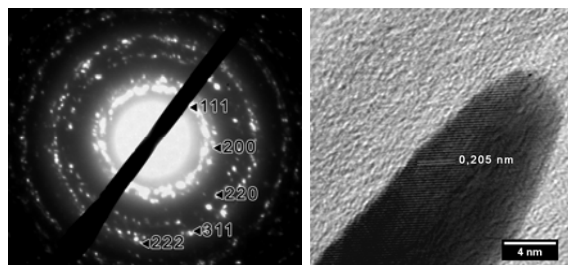


Figure 8: SAED (left) and HRTEM (right) of the elongated nano objects.

Interestingly, whatever the process employed and despite the differences between both architectures, the structure remains the same. The study was also completed by an XRD study on a layer of nanoparticles obtained after deposition of a concentrated solution on a substrate and evaporation of the solvent (figure 9).

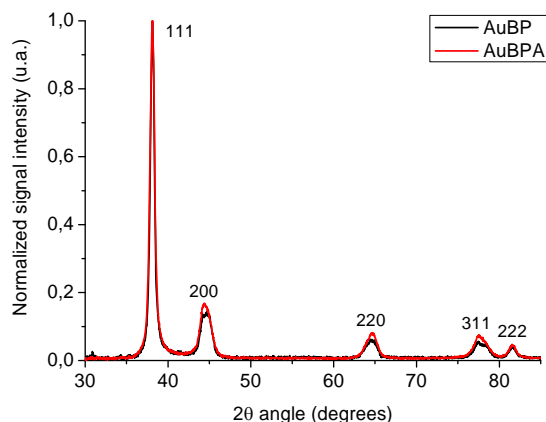


Figure 9: XRD of bipyramids and elongated particles after deposition of a concentrated solution on a substrate.

The diffractograms show a very intense signal related to the 111 plane compared to the others. Usually, for an isotropic gold particle with fcc structure, the ratio between 111 plane diffraction intensity and other planes is around 2 for 200, 3-4 for 220 and 311 and 10-15 for 222. Here the other diffractions peaks are three times lower in intensity and two times broader based on FWHM. This result clearly evidences the anisotropic growth of both kinds of particles along one preferential direction, typically the 100 plane. If we compare the diffractogram of bipyramids (AuBP) to the one of elongated bipyramids, the similarity is surprising. Normally, one would suppose that more anisotropic objects show higher difference between peaks intensities. Here, the ratio between 111 peak and other peaks is even slightly lower. The only difference is that the asymmetry of 220 and 311 peaks is more pronounced. We can suppose that the peculiar saw-tooth structure of the elongated particles is responsible for this behavior.

These results suggest a same configuration for these systems with a pentatwinned structure. The sharp shapes are due to the apparition of steps along the longitudinal axis leading to the tips. The main difference between bipyramids and elongated particles are the ways these steps are formed depending on the experimental parameters.

Growth mechanism

Among the many parameters influencing the final structure, the seed structure is determinant. It has already been shown that multiply-twinned seeds usually lead to bipyramids exhibiting a penta-twinned structure.³¹ here, based on our results; we can assume that during aging, the CTAC stabilized seeds turned from monocrystalline to polycrystalline with a penta-twinned structure.

Silver ions are essential in the growth of anisotropic structure, so are they in the case of our systems. Indeed no bipyramids were observed without Ag⁺ ions whether using CTAC or CTAB, in accordance to the literature.²⁶ The mechanism of silver(I) assisted growth is not yet unambiguously understood, but three main hypothesis can be found : an underpotential silver deposition,²⁶ a deposition of silver bromide on the gold surface³² or an interaction with a silver complex of CTAB.³³ In all these cases, the growth is inhibited on Au{110} faces leading the growth along the twinning axis of the seed on the Au{100} faces. On the other hand, the Br⁻ anions are known to adsorb predominantly on the Au{100} faces, slowing the growth on those faces. Therefore, the aspect ratio of the particle can be tuned by the balance between those two phenomena. Thus, a lower concentration of bromine ions would enhance the aspect ratio of bipyramids, but if the mechanism is based on a silver(I)-CTAB complex or a silver halide deposition on the faces, a minimal bromide or halide concentration is required to get bipyramids with high yield. Elongated nanoparticles with high aspect ratio can be obtained selectively by increasing the concentration of surfactant and replace most of CTAB by CTAC. A thorough control on the Cl⁻/Br⁻ ratio, allows to tune the aspect ratio and leads to strong variation in the LSPR (shifted up to 1000 nm compared to standard bipyramids) without varying the amount of gold seeds Jana N. et al.²⁵. This result also point out the importance of the aspect ratio and truncation of the particles.

Truncation

It is well established that LSPR varies with the aspect ratio of anisotropic nanoparticles. In our case, bipyramids behave the same way as nanorods: the higher the aspect ratio, the higher the LSPR. Although in the case of elongated bipyramids, the LSPR is much more sensitive to the aspect ratio. In fact, truncation and aspect-ratio are linked together, since truncation reduces aspect-ratio. By varying the truncation of gold bipyramids it is possible to play on the LSPR as well. Actually most of bipyramid synthesis in the literature plays on LSPR

modification because of differences in truncation, or in other term, the sharpness of the tips. In our case, the precise control on the bipyramids truncation was achieved using lower concentration of reducing agent (HQL figure 10) + (esi).

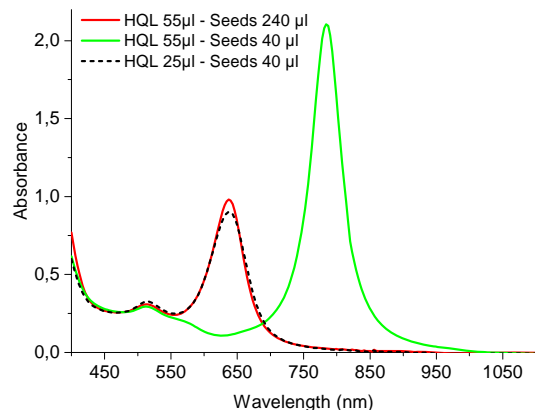


Figure 10 : SPR of the truncated bipyramids obtained from 55µl HQL + 240µl seeds (red) compared to small truncated bipyramids obtained with 25µl HQL + 40µl seeds (black dots) and normal bipyramids obtained with 55µl HQL + 40µl seeds (green).

This phenomenon can be explained by the low reducing efficiency of HQL. (HQL is a phenol but also a quinoline derivative, and interaction between the nitrogen and the O-H bond in a, very defavorable but existant lactim/lactam equilibrium, lowers the reducing power of the phenol function.) Therefore, a huge excess of HQL is needed to reduce gold quickly. If the reduction is too slow time because of low reducer concentration, a partial aging of bipyramids' tips may occur, displacing gold atoms toward the more thermodynamically stable center of the bipyramids, giving abnormally truncated bipyramids. This can be used to control the LSP while keeping the concentration of bipyramid constant, since the amount of seeds does not vary. Another interesting use of this phenomenon is to increase the amount of scattered light without varying the LSP, which can be useful for sensory applications. Gold nanobipyramids are always truncated, because of the instability of the tips, but the truncation can be more or less pronounced

It can be interesting to separate those two parameters, and one way to do it, is to calculate the "ideal" aspect-ratio of the non-truncated particle (figure 11).

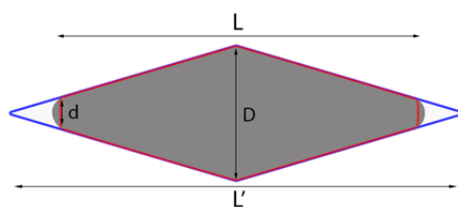


Fig. 11 : Illustration of bipyramid truncation : in gray, a truncated bipyramid compared to, in blue, an ideal non-truncated object. L is the tip to tip length of the truncated bipyramid, and L' the length of the non-truncated one. D is the central diameter of the bipyramid and d the diameter of the tips. L' can be calculated by $L' = L \cdot D / (D - d)$

The truncation can be easily calculated using the ratio of tip diameter and the central diameter of bipyramid. Based on figure 11, it is the ratio between the overall length of the non-truncated object and the central diameter, which is the same for the truncated and the ideal object. Since the length of the ideal object can be deduced from the diameters (tip and center) and length of the truncated bipyramids, it is easy to calculate this "ideal aspect-ratio". This is similar to using the tip angle [Geitner] but it can be tricky to measure on elongated bipyramids because of their wavy shape. Using the "ideal aspect-ratio" and the truncation, it is possible, for instance, to see a behavior in a synthesis. Those results can be correlated to theoretical calculation based on a square-based gold bipyramid

In order to analyse the experimental optical data, and gain additional information, theoretical spectra have been computed within the Discrete Dipole Approximation (DDA) which is a flexible numerical technique for determining optical properties of single or multiple nanoobjects of arbitrary shape or composition. Briefly the DDA method consists in replacing the nanoobject, and the embedding matrix if present, by a large set of polarizable points located in a cubic array (the polarizability in each material is set in relation to its corresponding bulk dielectric function). An applied linearly polarized plane wave gives these points a dipole moment, whose the characteristics (magnitude and direction) in the steady-state limit is ruled by the local field, namely the sum of the applied field and of the field radiated by all the other induced dipoles. The self-consistent coupled-dipole problem results in a very large system of 3N-coupled complex linear equations, which can be solved through iterative techniques. From the steady-state solution the internal and near fields, as well as the optical cross-sections, can be computed straight-forwardly. All the DDA spectra have been computed in using the code (version DDSCAT 7.2) developed by Draine and Flatau [1, 2], and a home-written code for generating truncated bipyramidal structures.

Besides the mesh size of the square dipole array and the shape of the nanoobject the input data in the modelling are the metal and matrix dielectric indexes. In our calculations the data from the Johnson and Christie gold table [3] and the matrix dielectric index $n_m=1.33$, appropriate for water in the spectral range of interest, have been used. Typically 1.6×10^5 dipoles have been taken for “filling” the truncated bipyramid-shaped gold nanoparticles (the total number of cubic cells in the computational domain (N) is of the order of $5-6 \times 10^5$). As emphasized in our previous work [4] assumptions concerning the bipyramid base are required for setting the particle geometry since the 2D-TEM images provide only projected particle shapes. For non-axially symmetric polygonal bases involving a small number of sides (triangle or square) the transverse dimension (parameter D in Figure 10) that is measured depends noticeably on the orientation of the bipyramid around its longitudinal axis. The D-value range is much narrower for polygonal bases involving a larger number of sides (pentagon for instance), especially when the bipyramid edges are strongly smoothed, as observed in our previous work by means of tomographic electron microscopy at the single-particle level [4]. In fact, for a given base area [and a given aspect ratio (AR)], the cross-sections depend only slightly on the number of sides of the high-order polygons. Moreover, for a fixed geometry, the longitudinal and transverse excitation spectra are not perceptibly modified when the bipyramid is turned around its long axis. In consequence a suitable approximation consists in assuming a circular base shape for carrying out the DDA computations. The length parameters of the truncated “bicone” geometry (see Figure 10), that is, L (overall physical length), D (diameter of the circular base) and d (diameter of the two circular apexes) have been deduced from TEM images (values averaged over several particles).

Since the extinction spectra from aqueous solutions are dominated by the strongly AR-dependent longitudinal excitation (electric field polarization along the bipyramid axis), we present only longitudinal spectra [the computed transverse spectra exhibit a weak and damped LSPR band around 520 nm and are quasi vanishing outside the interband transition spectral range. In all the spectra the longitudinal bands have a perfect Lorentzian curve shape, whose the maxima (λ_{RPS}) are found at (the aspect ratio $AR=L/D$ is given in brackets): 673 nm (2.25), 693 nm (2.4), 775 (2.75), 833 nm (3.1), 1050 nm (4.05) and 1500 nm (7.5). For the largest-AR geometry ($AR=11.1$) the limited spectral range of the Johnson and Christie table has prevented us from determining the spectral location of the LSPR band, which is nevertheless predicted to peak at much larger wavelength, as compared to the experiment. Except for the two largest-AR bipyramids the DDA spectra are in quasi perfect agreement with the experiment, supporting therefore the assumptions made regarding the modelling. The spectra of high-AR structures exhibit also small bumps in the left(blue)-hand side of the strong dipolar LSPR band, that can be attributed to the excitation of multipolar plasmon modes. The discrepancy noted for the bipyramids of high AR (larger than the linewidth; the linewidth of the LSPR band of the $AR=7.5$ -DDA spectrum (not shown) is about 170 nm) may have several origins. First TEM images show that the shapes of the high-AR elongated objects differ strongly from the diamond-like projected shapes of the low-AR bipyramids (javelin-like overall shape with a pronounced irregular surface). Second, the shape of the high-AR bipyramids cannot be “perfectly” modeled in the DDA calculations, as compared to that of the low-AR structures. Actually, because of the space discretization in the DDA approach, the effective shape of the large set of small cubic cells filling the perfect bipyramidal shape looks like the stacking of constant-height slabs whose the transverse shape is that of the base. For very elongated particles the number of involved slabs in each half-bipyramid turns out to be insufficient for ensuring a sufficient smoothing of the intrinsic roughness of the DDA-structures (in particular the apexes in the bicone structures are cylinders with a rough surface). Because the computation time increases dramatically, on the one hand when the number of cells in the computational domain is enlarged (multi-plying the number of slabs by two amounts to increasing N by a factor 8), and, on the other hand because of the slow convergence in the IR spectral range (much more 500 iterations are required), we were unable to assess this possible explanation.

Further information can be gained in analysing the linewidths of the LSPR bands on the energy scale. In view of the large particle sizes involved in this work both intrinsic losses (intraband and inter-band excitations) and extrinsic losses (radiative damping) contribute a priori to the damping of the collective plasmon excitation, in other terms the LSPR broadening. The interband mechanism, yielding to the formation of excited electron-hole pairs (d band \rightarrow sp conduction-band electronic transitions), can be disregarded since the LSPR energies ERPS are far below, or very close to, the interband transition threshold. Lorentzian-shaped curve fitting of the LSPR bands leads to the following values (in meV): 100 ($AR=2.25$), 103 (2.4); 127 (2.75), 113 (3.1), 134 (4.05) and 93 (7.5). For estimating the respective contributions of the nonradiative and radiative damping processes we have computed extinction cross-sections of small matrix-embedded gold spheres within the quasistatic limit (extinction = absorption) for increasing value of the matrix index in order to shift the LSPR towards the low energy part of the spectrum, below the interband transition threshold. LSPR linewidths on the order of 70-75 meV, that are entirely ruled by the intraband excitations (in a classical picture this loss channel corresponds to electron scattering processes within the nanoparticle), are obtained. These results indicate that the major part of the extinction for bipyramids, in the size range studied, is exhausted by intrinsic intraband-related losses (absorption), as supported by the DDA calculations. As expected the relative contributions of absorption and scattering are correlated to a great extent to the volume of the bipyramids. For instance the structures having the highest ($AR=4.05$) and smallest ($AR=2.25$) ratio are those having the largest and smaller volumes, 91356 nm³ and 3656 nm³, respectively. Analysis of the experimental spectra (Figures 3 and 4) shows that the experimental linewidths are on the same order of magnitude as those computed for a single particle, proving the high monodispersity of the solutions during the growth process.

As emphasized previously, the geometry of the bipyramids, and concomitantly the plasmonic response, depend on several -some of them non-independent- parameters, as the physical AR, the degree of truncation with respect to a fictitious ideal non-truncated bipyramid, the overall volume, the base shape. Actually, the physical AR, parameter that can be defined for any kind

of elongated nano-particle, contrary to the degree of truncation, turns out to be the relevant and ideal parameter for correlating the plasmonic response (on the wavelength scale) with the geometrical structure. Except for the two largest-AR structures the wavelength of the resonance is clearly found to vary linearly with the aspect ratio, as observed also for nanorods [5], though the degrees of truncation (see Table 1) and the volumes of the five structures differ strongly [the volumes are respectively (in nm³): 3656 (AR=2.25), 8338 (2.4), 20175 (2.75), 22671 (3.1) and 91356 (4.05)], pointing out the relevance of the AR parameter for rationalizing the optical data. For largest aspect ratios the nonlinear evolution is qualitatively similar to that observed in ref [6], but, from a quantitative point of view, the λ_{RPS} -curves are different. In the context of the labelling and sensing applications discussed in the introduction the bipyramidal shape is of particular interest due to the larger sensitivity of λ_{RPS} to the aspect ratio, in addition to the high quality factor of the resonance, in comparison with other kinds of elongated particle shapes. The slope is on the order of 200 nm, twice larger than that for nanorods [5] or prolate spheroids. Note that, as compared to bipyramidal shapes, the linear law is obeyed in a broader AR range (the slight deviation for small AR values results from the overlapping between the LSPR band and the rising edge of the interband transitions).

The theoretical results concern perfect bicone structures. One may wonder whether this linear behavior can be “extrapolated” to bipyramids with other base shapes. As implicitly stressed before, defining an aspect ratio is “problematic” for non-circular shapes, as polygons, and its definition has to be grounded -as much as possible- on a physical basis. For fixed geometry and irradiation conditions, calculations show that the cross-sections, in particular the location of the LSPR band, are insensitive to the orientation of the bipyramid around its long axis. This suggests strongly that the base area S is a relevant parameter. It is thus natural to define the transverse dimension as the diameter of the disk of equal area, all the more that with such a definition all the base shapes are treated on an equal footing. For illustrating this ansatz we have performed computations in assuming that the transverse dimension measured by TEM (that is D) is the side (denoted a ; $S=a^2$) of the base of square-base bipyramids. Lorentzian-shaped curve fitting of the LSPR bands in the DDA spectra yields the following LSPR maxima (in nm): 651, 672, 737, 794, 994 and 1401. Except for the two extreme values the agreement with the experimental data are poorer, as compared to the bi-cone λ_{RPS} -values, supporting the suitability of this simple axially-symmetric structure for predicting the plasmonic response. For these square-base bipyramids the effective aspect ratio is equal to where L/D is the (observed) aspect ratio determined from the TEM images. The corresponding λ_{RPS} -values are plotted in Figure Bb (empty squares), together with the bicone λ_{RPS} -values (red crosses). All the data are approximately “aligned” along a common curve, pointing out the relevance of this general definition. Actually, thanks to this robust AR-dependency, the transverse area can be determined approximately from the experimental spectral position of the LSPR band.

Finally we report on the sensitivity of the results on the dielectric matrix index N_m . Six truncated square-base bipyramids, embedded in a matrix of dielectric index $N_m=1.4$, have been generated in truncating progressively a perfect (ideal) bipyramid with $L'=170$ nm (see Figure 10 for the definition of L') and $a = 40$ nm (side of the square base). The six degrees of truncation are characterized by $d(\text{nm}) = 4, 8, 12, 16, 20$ and 24 (see Figure 10). The DDA extinction spectra have been displayed in the Figure 9 in our previous work ref 4. As in water ($N_m=1.33$) the points are aligned along a straight line, except those corresponding to low AR-values because of the overlapping of the LSPR band with the interband transitions. The sensitivity to the matrix index clearly supports the selected value for modelling the dielectric properties of water in the visible and IR spectral ranges. In order to analyse the experimental optical data, and gain additional information, theoretical spectra have been computed within the Discrete Dipole Approximation (DDA) which is a flexible numerical technique for determining optical properties of single or multiple nanoobjects of arbitrary shape or composition. Briefly the DDA method consists in replacing the nanoobject, and the embedding matrix if present, by a large set of polarizable points located in a cubic array (the polarizability in each material is set in relation to its corresponding bulk dielectric function). An applied linearly polarized plane wave gives these points a dipole moment, whose the characteristics (magnitude and direction) in the steady-state limit is ruled by the local field, namely the sum of the applied field and of the field radiated by all the other induced dipoles. The self-consistent coupled-dipole problem results in a very large system of 3N-coupled complex linear equations, which can be solved through iterative techniques. From the steady-state solution the internal and near fields, as well as the optical cross-sections, can be computed straightforwardly. All the DDA spectra have been computed in using the code (version DDSCAT 7.2) developed by Draine and Flatau, and a home-written code for generating truncated bipyramidal structures.

CONCLUSION

These types of elongated structures with high aspect ratio allowed more important extension of the LSPR towards the IR wavelengths, as far as 1850nm. To the best of our knowledge, thin LSPR at such wavelength have never been reached before with these kinds of nano-objects, opening the perspective to important application in the IR wavelengths.

REFERENCES

- (1) Anger, P.; Bharadwaj, P.; Novotny, L. Phys. Rev. Lett. 2006, 96, pp 3–6
- (2) Saute, B.; Narayanan, R. Analyst 2011, 136, pp 527–532

- (3) Le Ru, E. C.; Grand, J.; Sow, I.; Somerville, W. R. C.; Etche-goin, P. G.; Treguer-Delapierre, M.; Charron, G.; Felidj, N.; Levi, G.; Aubard, J. *Nano Lett.* 2011, 11, pp 5013–5019
- (4) Thakor, A. S.; Jokerst, J.; Zavaleta, C.; Massoud, T. F.; Gam-bhir S. S. *Nano Lett.* 2011, 11, pp 4029–4036
- (5) Huang, X.; Jain, P. K.; El-Sayed, I. H.; El-Sayed, M. A. *Nano-medicine* 2007, 2, 681–93
- (6) Navarro, J.R.G.; Lerouge, F.; Cepraga, C.; Micouin, G.; Favier, A.; Chateau, D.; Charreyre, M.-T.; Lanoe, P.-H.; Monnereau, C.; Chaput, F.; Marotte, S.; Leverrier, Y.; Marvel, J.; Kamada, K.; Andraud, C.; Baldeck, P.L.; Parola, S. *Biomaterials*, 2013, 34, pp 8344–8351
- (7) Narayanan, R.; El-sayed, M. A. *J. Phys. Chem. B* 2005, 109 (26), pp 12663–12676
- (8) Narayanan, R.; El-Sayed, M. A. *Nano Lett.* 2004, 4 (7), pp 1343–1348
- (9) Zaiba, S.; Lerouge, F.; Gabudean, A.-M.; Focsan, M.; Lermé, J.; Gallavardin, T.; Maury, O.; Andraud, C.; Parola, S.; Baldeck, P. L. *Nano let.* 2011, 11, pp 2043–2047
- (10) Tam, F.; Goodrich, G. P.; Johnson, B. R.; Halas, N. J. *Nano lett.* 2007, 7, pp 496–501
- (11) Bardhan, R.; Grady, N. K.; Cole, J. R.; Joshi, A.; Halas, N. J. *ACS Nano* 2009, 3, pp 744–752
- (12) He, R.-Y.; Cho, K.-C.; Chang, N.-S.; Su, Y.-D.; Chen, S.-J. *Proceedings of SPIE* 2009, 7183, 71831L–71831L–9
- (13) Thomas, M.; Greffet, J.J.; Carminati, R.; Arias-Gonzales, J.R. *Appl. Phys.Lett.* 2004, 85 (17), pp 3863–3865
- (14) Thomas M. PhD Thesis, University Orsay Paris XI, 2004
- (15) Navarro, J. R. G.; Lerouge, F.; Micouin, G.; Cepraga, C.; Favier, A.; Charreyre, M.-T.; Blanchard, N. P.; Lermé, J.; Chaput, F.; Focsan, M.; Kamada, K.; Baldeck P. L.; Parola, S. *Nanoscale* 2014, 6, pp 5138
- (16) Chen, Y.; Munechika, K.; Ginger, D. S. *Nano let.* 2007, 7, pp 690–696
- (17) Grzelczak, M.; Pérez-Juste, J.; Mulvaney P.; Liz-Marzan L. M. *Chem. Soc. Rev.* 2008, 37, pp 1783–1791
- (18) Long, N. N.; Vu, L. V.; Kiem, C. D.; Doanh, S. C.; Nguyet, C. T.; Hang, P. T.; Thien, N. D.; Quynh, L. M. *Journal of Physics: Conference Series* 2009, 187, p 012026
- (19) Rai, A.; Chaudhary, M.; Ahmad, A.; Bhargava, S.; Sastry, M. *Materials Research Bulletin* 2007, 42, pp 1212–1220
- (20) Murphy, C. J.; Sau, T. K.; Gole, A. M.; Orendorff, C. J.; Gao, J.; Gou, L.; Hunyadi, S. E.; Li, T. J. *Phys. Chem. B* 2005, 109, pp 13857–13870
- (21) Sivapalan, S. T.; Vella, J. H.; Yang, T. K.; Dalton, M. J.; Swiger, R. N.; Haley, J. E.; Cooper, T. M.; Urbas, A. M.; Tan, L.-S.; Murphy, C. J. *Langmuir* 2012, 28, pp 9147–9154
- (22) Kumar, P. S.; Pastoriza-Santos, I.; Rodriguez-Gonzalez, B.; Garcia de Abajo, F. J.; Liz-Marzan, L. M. *Nanotechnology* 2008, 19, 015606
- (23) Kou, X.; Ni, W.; Tsung, C.-K.; Chan, K.; Lin, H.-Q.; Stucky, G. D.; Wang, J. *Small* 2007, 3 (12), pp 2103 – 2113
- (24) Navarro, J. R. G.; Manchon, D.; Lerouge, F.; Cottancin, E.; Lermé, J.; Bonnet, C.; Chaput, F.; Mosset, A.; Pellarin, M.; Pa-rola, S. *Nanotechnology* 2012, 23, 145707
- (25) Jana, N. R.; Gearheart, L.; Murphy, C. J. *Advanced Materials* 2001, 13, pp 1389–1393
- (26) Liu, M.; Guyot-Sionnest, P. J. *Phys. Chem. B* 2005, 109, pp 22192–22200
- (27) Ha, T. H.; Koo, H.-J.; Chung, B. H. J. *Phys. Chem. C.* 2007, 111, pp 1123–1130
- (28) Millstone, J. E.; Wei, W.; Jones, M. R.; Yoo, H.; Mirkin, C. A. *Nano let.* 2008, 8, pp 2526–2529
- (30) Geitner, N.K.; Doepke, A.; Fickenscher, M. A.; Yarrison-Rice, J. M.; Heineman, W. R.; Jackson, H. E.; Smith, L. M. *Nanotechnology* 2011, 22, pp 275607
- (31) Kou, X. et al. *J Phys. Chem. B* 2006, 110, pp 16377–16383.
- (32) Murphy, C.J. et al. *Current Opinion in Colloid & Interface Science* 2011, 16, pp 128–134.
- (33) Hubert, F.; Testard, F.; Spalla, O. *Langmuir* 2008, 24, pp 9219–9222.

2/ Dispersion and self-orientation of gold nanoparticles in sol-gel hybrid silica – optical transmission properties

Silica based hybrid materials doped with gold nanoparticles of different shapes (AuNPs) were prepared with an adapted sol-gel technology (using MTEOS) and polished to high optical quality. Both spherical (23 and 46 nm in diameter) and bipyramidal (36, 50 and 78 nm in length) AuNPs, were prepared and used as dopants. They were functionalized with an original silicon polymer for compatibilization with the sol-gel medium. The glass materials showed well defined localized surface plasmon resonance (LSPR) absorbance from the visible to NIR. No redshifts in the spectra, due to the increase in doping concentration, were observed in the glasses, proving that no or very small LSPR coupling effects occurred. Spectroscopic Muller Matrix Ellipsometry showed that the shorter bipyramidal AuNPs (36 and 50 nm in length) have a clear preferred orientation in the MTEOS matrix, i.e. a tendency to be oriented with their long axis in the plane parallel to the glass surfaces. This can induce important impacts in the

optical responses, in particular nonlinear properties. Dispersions of AuNPs have proven to be good optical limiters that depend on particle size and geometry. The solid-state glass materials showed good optical limiting at 532 nm for nanosecond pulses, which did not depend on size or geometry of the AuNPs. For wavelengths at 600 nm no optical limiting effect was observed. The preferred orientation of the smaller AuNPs, in the MTEOS matrix, has no major impact on the optical limiting. As for AuNPs in liquids, the dominant mechanism behind the optical limiting response for the solids reported here is scattering.

Introduction

Gold nanoparticles (AuNPs) attract much attention due to their chemical stability and the various possibilities to prepare different architectures (spheres, cubes, rings, rods, stars, bipyramids, shells, cages, etc).¹⁻¹² One of the main reasons of such interest is the ability to control their localized surface plasmon resonance (LSPR) absorption depending on the shape, size and coupling to the dielectric environment of the particles.¹³ The LSPR absorption is a manifestation of the free electrons in the conduction band of the nanoparticle, which collectively oscillate upon interaction with optical radiation. Depending on the size and shape of AuNPs it can be controlled for wavelengths ranging from Vis to NIR.^{5,14,15} This ability to tune the optical properties gives new opportunities for advanced photonic technology. In the past years, one area of intense research has been optical limiters for nonlinear control of optical transmission. The LSPR absorption, being a nanoparticle phenomenon, has therefore given new ways to obtain effective optical limiters. Thus AuNPs have been widely studied for this application.¹⁶⁻²⁸ Dispersed in organic solvents the AuNPs act as optical limiters, mostly due to laser-induced fusion or refractive index variations leading to light scattering centers^{28,29} or for smaller units, approximately 3 nm, free-carrier absorption.³⁰ For nanosecond laser pulses, at 532 nm, the AuNPs show size and geometry dependent optical limiting response, with a better efficiency for larger particles, up to a certain size.^{16,18-21,31} This optical limiting response for AuNP dispersed in solids also decreases with increasing wavelength.²⁸ Meneghetti and co-workers showed that for such dispersions, laser-induced fission leads to a lowering of the optical limiting effect due to depletion of larger more effective AuNPs.²⁶ They also showed that Zinc phthalocyanines can prevent the laser fission process and thus, no hampering of the optical limiting effect was observed.

Nanoparticles in liquids are not suitable for field/real applications as the particles have a tendency to either aggregate and/or precipitate.¹⁷ Therefore, stable solid-state materials need to be developed for more practical applications. Solid-state materials can be made as thin-films or monoliths by low-temperature preparation methods such as sol-gel or polymerization of organic precursors. Though there are in general some drawbacks with solid-state optical limiting materials in comparison with dispersions and solutions; they have lower damage thresholds and are less effective dispersed in solid matrices such as SiO₂ and PMMA.^{32,33} OPL investigations of AuNP solid-state materials are scarce and have only recently appeared in the literature. AuNP thin-film nanocomposites have, as for the dispersions and nanosecond pulses, also shown scattering as the main mechanism for optical limiting.²¹ For example, monolithic glass materials doped with AuNPs have been prepared through laser irradiation of glass materials containing Au₂O.²⁵ Samples prepared with this technique showed LSPR absorption bands from 528 to 534 nm, and free-carrier absorption was concluded to be the mechanism for nonlinear absorption.

In this study we describe a new sol-gel approach to prepare bulk materials doped with different sizes of polymers, coated AuNP spheres and bipyramids. The preparation method gives materials in which bipyramids to various extents are self-oriented in the matrix. The resulting glass materials can be cut and polished to high optical quality, a property that is central for real optical applications. We report on nonlinear optical response and spectroscopic ellipsometric measurements in addition to general material characterization.

Experimental

Diethoxydimethylsilane, (3-mercaptopropyl)-methyl-dimethoxysilane, (3-glycidoxypopyl) -methyl-dimethoxysilane, HCl, triethylamine, ethanol, THF, diethyl ether, MTEOS, citric acid, CTAC 25 % in water, HAuCl₄·3H₂O, NaBH₄, NaOH and APTES are purchased from Sigma-Aldrich and used as received. The detailed preparations and purification of the AuNPs are described elsewhere.^{4,6,9,14,15}

Synthesis of the gold spherical nanoparticles

The spherical nanoparticles were prepared following the seeds mediated growth approach allowing very low polydispersity of the samples (Figure 1). The seeds were first prepared by quickly injecting 400 μ L of a freshly prepared NaBH₄ 50 mM/NaOH 50mM mixture into a solution consisting in 32mL cetylpyridinium chloride monhydrate (CTAC 66mM), 320 μ L of HAuCl₄ (25mM in water) and 296 μ L of HNO₃ (0,25M), under vigorous stirring. After 1 min stirring was stopped and the solution was heated at 80°C during 50 min. The growth solution was prepared by adding 600 μ L of CTAC and 200 μ L of HAuCl₄ (25 mM) into 19.4 mL of highly pure water. The mixture was then stirred 15 min at 60°C before adding 150 μ L of HQL (0.4M in THF). Finally, spherical gold nanoparticles were synthesized by adding the appropriate amount of seeds in the growth solution in order to obtain the desired size. For example, 45 nm particles were obtained by adding 120 μ L of the seeds solution in the growth solution.

Synthesis of the bipyramidal nanoparticles

Preparation of the seeds: To a solution of CTAC 66mM in 8mL of water, were added under stirring, 80 μ L of HAuCl₄ 25mM and 74 μ L of HNO₃ 0.25M. The mixture was stirred vigorously before adding 100 μ L of NaBH₄ 50mM / NaOH 50mM followed by 80 μ L of citric acid 1M. The mixture was aged in water bath at 80°C for 50 mn.

Preparation of the bipyramids: A solution was prepared with 4 mL CTAB (16.5 g.L⁻¹ in H₂O), 40 μ L HAuCl₄ (25 mM in H₂O), 35 μ L AgNO₃ (5 mM in H₂O), 60 μ L HQL (0.4M in THF) and the adapted volume of the seeds solution depending on the size of the bipyramids, typically 180 μ L for LSPR@640 nm, 75 μ L for LSPR@700 nm and 30 μ L for LSPR@770 nm (Figure 1). The vessel was closed and aged in oven at 45°C for 1h.

Preparation of functional polymer

8,3mL (46,95 mmoles) of diethoxydimethylsilane, 760 μ L (4,18 mmoles) of (3-mercaptopropyl)-methyl-dimethoxysilane and 780 μ L (3,62 mmoles) of (3-glycidioxypropyl)-methyl-dimethoxysilane were mixed together in a round bottom flask, equipped with a condenser, containing 4mL MilliQ water and 40 μ L HCl (0,1 M). After 20 minutes of stirring at room temperature, 380 μ L of triethylamine (2,7 mmol) was added. The mixture was then refluxed at 120°C (bath temperature) for two hours. Finally, the condenser was replaced with a distillation apparatus, and the mixture heated for two more hours, to remove the solvents and improve the reticulation of the polymer (Figure 2). The final residue is dispersed in ethanol (30 ml) for storage.

¹H NMR (300 MHz, CDCl₃) δ 3.92 – 3.81 (m, \approx 1H), 3.59 – 3.43 (m, \approx 2H), 3.50 – 3.38 (m, \approx 2H), 2.74 – 2.56 (m, \approx 2H), 2.65 – 2.46 (m, \approx 2H), 1.81 – 1.53 (m, \approx 4H), 1.33 (t, J = 7.1 Hz, \approx 0.3x1H), 0.72 – 0.54 (m, \approx 2H), 0.60 – 0.41 (m, \approx 2H), 0.19 – 0.02 (m, \approx 6H+13x6H).

²⁹Si NMR (99 MHz, Acetone) δ -13.62 (D1 OH), -14.18 (D1 OH), -14.98 (D1 OH), -19.19(cycles D4), -21.93 à -22.21 (D2), -22.83 (D2).

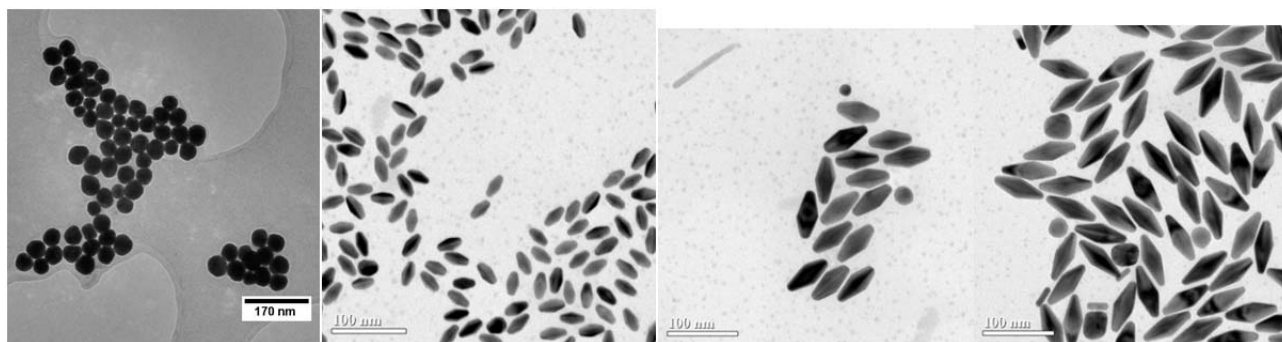


Figure 1: TEM images of respectively from the spherical (top left 45 nm) and bipyramidal (LSPR@640 (top right), 700 (bottom left), 770 nm (bottom right)) gold nanoparticles.

Functionalization of particles and extraction in THF

100 μ L of polymer diluted to 1% in ethanol was mixed with 4 mL of gold nanoparticles (0,25 mM in Au⁰ for gold bipyramids and 0,5mM for gold spheres, purified only one time by centrifugation after synthesis). The mixture was sonicated during 5 minutes and incubated at 45°C during 72h. The dispersion was then cooled down to RT and 4 ml of THF was added under stirring, followed by 0.8 ml of diethyl ether to provoke phase separation. Stirring is stopped after one minute, and a clear aqueous phase separates from a particles colored organic phase. The aqueous phase is discarded and THF is added to the organic phase to get a final volume of 4 ml. Scanning Electron Microscopy (SEM) images of functionalized bipyramids are shown in figure 3.

AuNP	Reference	[Au ⁰] (mM)	Volume of functionalized particles' solution added	Calculated [AuNP]
Spheres 23 nm.	AuNP-S1	0.125	75μl	0.06 nM
	AuNP-S2	0.25	150μl	0.13 nM
	AuNP-S3	0.50	300μl	0.25 nM
	AuNP-S4	1.00	600μl	0.5 nM
Spheres 45 nm	AuNP-S10	0.031	18.8μl	0.006 nM
	AuNP-S11	0.063	37.5μl	0.013 nM
	AuNP-S12	0.125	75μl	0.026 nM
	AuNP-S13	0.25	150μl	0.052 nM
	AuNP-S14	0.50	300μl	0.1 nM
Bipyramids LSPR@640nm	AuNP-B31	0.063	75μl	0.29 nM
	AuNP-B32	0.125	150μl	0.58 nM
	AuNP-B33	0.25	300μl	1.15 nM
Bipyramids LSPR@700nm	AuNP-B41	0.063	75μl	0.12 nM
	AuNP-B42	0.125	150μl	0.24 nM
	AuNP-B43	0.25	300μl	0.48 nM
Bipyramids LSPR@770nm	AuNP-B51	0.063	75μl	0.048 nM
	AuNP-B52	0.125	150μl	0.097 nM
	AuNP-B53	0.25	300μl	0.19 nM

AuNP / LSPR	Mean particle size/dimensions (D,L, and tip diameter in nm)
Spheres LSPR 530 nm	23 nm diameter (DLS)
Spheres LSPR 535 nm	45 nm diameter (DLS)
Bipyramids LSPR 640 nm	16 ± 2 ; 36 ± 2 ; 6 ± 1
Bipyramids LSPR 700 nm	21 ± 2 ; 50 ± 2 ; 8 ± 1
Bipyramids LSPR 770 nm	28 ± 3 ; 78 ± 2 ; 8 ± 1

Monolithic materials preparation

The desired amount of functionalized AuNP in THF was added to 1g of the sol. The mixture was placed in a PTFE mould and 45 μL of APTES added to induce a fast condensation of the sol. The gel was formed after a few minutes. After gelation, the loaded mould was closed and put in a drier. The gel was slowly dried for 48h at 45°C and for another 24h at 80°C. Table 1 summarizes the prepared sol-gel materials. Examples of the prepared crude materials are shown in Figure 4.

For spheres, concentrations were estimated based on extinction coefficient and absorbance spectra of starting solutions. For bipyramids, a truncated biconic shape was used to get the volume and the number of gold atoms per particle, and incidentally, the number of particles for a definite [Au⁰]. A density of 1.21 measured by buoyancy method on an undoped material was used to calculate its volume and deducing the concentration of particles inside the matrix.

Cutting and Polishing

The glasses were cut with a Buehler Isomet 1000 precision saw. They were then polished to a thickness of 1±0.05 mm with a Struers polishing equipment.



Figure 4. Example of crude glass materials; AuNP-S1 – AuNP-S4 (top row) and AuNP-S10 – AuNP-S14 (bottom row).

Measurements

UV-Vis spectra were recorded either with a CARY 5G UV-Vis-NIR spectrophotometer or Perkin-Elmer UV-Vis-NIR Lambda 750 spectrometer. Transmission electron microscopy (TEM) images for the AuNPs were obtained using a TOPCON EM-002B microscope (120 kV).

Spectroscopic ellipsometry was performed in the transmission geometry with the commercial Spectroscopic Mueller Matrix Ellipsometer from the JA Woolam Company (RC2). The samples were measured with a collimated beam in transmission with incidence angles ranging from 0-75 degrees in steps of 5 degrees.

The optical power limiting measurements (OPL) were carried out with a Quantel Brilliant B Nd:YAG laser with a pulse-length of approximately 5 ns. This was then frequency doubled to 532 nm (SHG) or upconverted to 600 nm beam using an optical parametric oscillator. The laser beam was focused through a pinhole to reduce the spatial imperfections of the beam. The energy of the laser pulses were attenuated by up to OD 3 in OD 0.1 steps by combining neutral density filters placed in two filter wheels. To record the energy of each laser pulse an 8% pellicle beamsplitter was used to redirect a proportion of the pulse energy to the reference detector, an Ophir PE9 laser energy meter. The main laser beam was then expanded by a 2X Galilean beam expander to fill the 20 mm aperture in front of a 100 mm focal length achromatic doublet focusing the beam into the glass sample. The glass sample was shifted slightly in a direction perpendicular to the beam between each pulse. This to avoid laser induced damages by repeated focusing on the very same spot of the glass material. The beam transmitted through the glass sample was then re-collimated by a 40 mm focal length achromatic lens, passed through an 8 mm diameter aperture, and finally focused again onto the signal detector (Ophir PD10-V1-SH laser energy meter).

The input fluence (J/cm^2) at the focus in the glass was estimated from the reference signal by two calibration measurements. The signal detector was placed slightly in front of the sample's position to find the factor between measured reference energy and energy on the glass sample. The area of the beam was estimated with the 10/90 knife edge method, assuming a top-hat beam. The beam diameter was measured to be 8.25 μm and 20.5 μm at 532 and 600 nm wavelengths, respectively.

The integrating sphere measurements were made with the same setup and calibration procedure as in the optical power limiting measurements, but with the rear lenses and aperture removed. A 75 mm diameter integrating sphere was positioned around the glass sample with its entrance towards the incoming light beam and its output placed perpendicular to the optical axis. The signal detector was placed against the integrating sphere's output opening. The measured pulse energy is assumed linear to scattered and transmitted energy. To minimize the collection efficiency difference between scattered and transmitted light, the thin sample holder was painted with white paint. The integrating sphere was calibrated by measuring the output energy for different input fluence.

Results and discussion

In this article preparation of AuNP nanocomposites is described, which give glass materials that can be cut and polished to high optical quality (Figure 5). The nanoparticles were prepared using seed mediated synthesis which allows high yield and monodispersity. The nanoparticles were then functionalized using a silicon based polymer which allows high compatibility between the gold systems and the hybrid silica matrices. The nanoobject were finally introduced in the hybrid silica based matrices using the sol-gel process after controlled hydrolysis of methyltriethoxysilane precursors and a fast condensation step using aminopropyltriethoxysilane. This method was previously used to entrap efficiently high concentration of organic or organometallic dyes.^{32,34}

The transmission spectra showed well-defined plasmon absorption peaks, indicating a narrow size distribution of the AuNPs (exemplified in Figures 6 and 7). As expected, the bipyramids showed a second small absorption peak at a shorter wavelength, due to the transversal plasmon oscillation. As can be seen in Figure 7 an increase in AuNP concentration showed no (or marginal) wavelength shifts of the plasmon resonance peaks for both spheres and bipyramids.

Dispersions of AuNPs in liquid, on the other hand, have been reported to show LSPR coupling leading to a redshift of the absorbance due to proximity of almost aggregated particles.¹³

In the prepared solids reported here there is no indication of redshifts in the optical absorption as the concentration of the AuNPs increases. This shows that there is no or very small LSPR coupling effects in the solid glasses. The only redshift that is observed is attributed to size effects. The lack of LSPR coupling could allow for more highly doped glasses, with plasmon resonance properties preserved at the wavelengths associated to the individual particles.

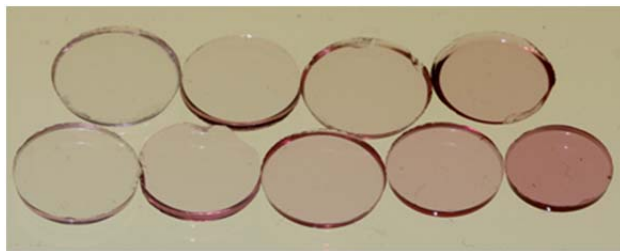


Figure 5. Example of cut and polished AuNP nanocomposites; AuNP-S1 – AuNP-S4 (top row) and AuNP-S10 – AuNP-S14 (bottom row).

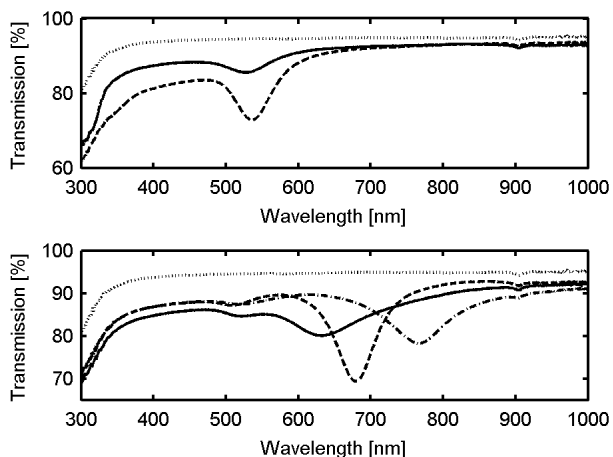


Figure 6. Transmission spectra for AuNP nanocomposites. The concentration of Au⁰ in the glasses shown in these plots are 0.125 mM. The dotted lines in both plots represent a pure MTEOS glass. The upper plot shows spherical gold nanoparticles with a diameter of 23 nm, AuNP-S1, (solid line) and 45 nm, AuNP-S12, (dashed line). The lower plot shows bi-pyramidal gold nanoparticles with a plasmon at 640 nm, AuNP-B32 (solid line), 700 nm, AuNP-B42 (dashed line) and 770 nm, AuNP-B52 (dash-dotted line).

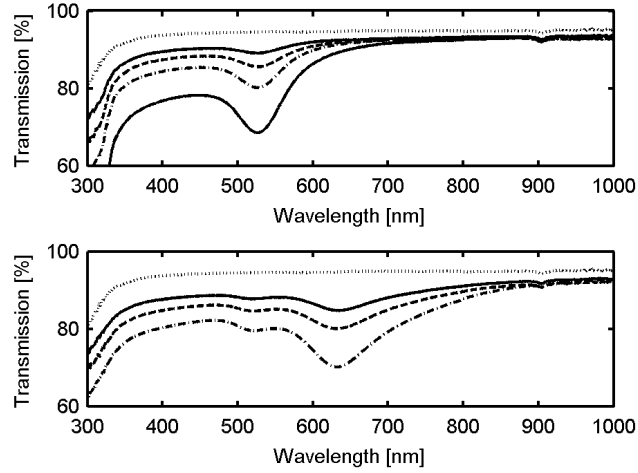


Figure 7. Transmission spectra for AuNP, 45 nm spheres (AuNP-S10 – AuNP-S14, upper plot), and bi-pyramid, LSPR @ 640 nm (AuNP-B31 – AuNP-B33, bottom plot), at different doping concentrations (table 1).

The pore shape of silica nanofibers can orientate nonspherical AuNPs.³⁵ It was therefore of interest to determine if the pores in silica could act in a similar way in the monoliths prepared here even if it was previously demonstrated that only micropores were observed in such matrix.³² For this investigation we employed Spectroscopic Muller Matrix Ellipsometry, which is sensitive to ordered (or partially ordered) anisotropic plasmonic particles. The overall optical response described by the Muller Matrix was found to be largely block-diagonal, and hence the resulting transmission Jones matrix is approximately diagonal:

$$\begin{bmatrix} t_p & 0 \\ 0 & t_s \end{bmatrix} = t_s \begin{bmatrix} \tan \psi \exp i\Delta & 0 \\ 0 & 1 \end{bmatrix} \quad (1)$$

As a consequence, we can focus on the standard ellipsometric parameters ψ and Δ , and we discuss in particular ψ . Furthermore, in this case $m_{12}=\cos 2\psi$, $m_{33}=\sin 2\psi \cos \Delta$ and $m_{34}=\sin 2\psi \sin \Delta$. Hence, the ellipsometric parameters can be unambiguously determined from the measured Mueller matrix elements (i.e. standard transmission ellipsometry). Figure 8 shows the ellipsometric parameter, ψ , for the bi-pyramidal AuNP samples at the highest concentrations, and show clear plasmon resonances. From the measured Mueller matrix (not shown) a clear plasmon related peak was observed in the m_{12} element with a corresponding dip in the m_{34} element for the AuNP-B33 and AuNP-B43. A small peak was also observed in the m_{33} element. The amplitude of these peaks and dips increased as a function of incidence angle, but the energy position of the resonances do not change. The remaining off-diagonal elements were found to be negligible around the plasmon resonances. Figure 8 shows thus that the attenuation of the probing beam, through the sample, at 45o angle of incidence, clearly differ for the s and p-polarized component of the electric field. Let us describe the Jones matrix of the sample, by an attenuation of the s and p component using a simple “Bio-Savart” type law:

$$J = \begin{bmatrix} (1-R_p)e^{-\alpha_p} & 0 \\ 0 & (1-R_s)e^{-\alpha_s} \end{bmatrix} \quad (2)$$

where $R=(r_{01})^2$, r_{01} is the Fresnel reflection coefficient between the ambient/bulk glass interface, with subscripts s and p for s or p-polarized light, respectively. This gives

$$\tan \psi = \frac{|t_p|}{|t_s|} = \frac{|1 - R_p| e^{-\alpha_p}}{|1 - R_s| e^{-\alpha_s}} \quad (3)$$

a quantity also calculated directly from the measured Mueller Matrix. Equation (3) shows that the overall featureless response is mainly a “Brewster effect” from the interfaces, while a peak in ψ (or a peak in $\tan \psi$) must be the result of a peak in α_s , i.e. an increased absorption for the E-field component perpendicular to the incidence plane (i.e. parallel to the glass surfaces). Similarly, a dip in ψ must be the result of a peak in α_p . Note that the attenuation described by α_p conveys both a component perpendicular and parallel to the sample surface, and its magnitude is also dependent on path length, both dependent on incidence angle. In terms of anisometric shaped plasmonic particles, the bottom plot in Figure 7 shows the well-known fact that the long axis of the particle result in a red-shift of the plasmon resonance, while the short axis result in a blue shift of the resonance. The energy-position of the resonances giving a peak in ψ , are thus a result of the localized plasmon with the E-field along the long axis (parallel to the particle). Similarly, a careful inspection of Figure 8, shows a small dip in ψ , corresponding to the blue shifted resonance, i.e. a resonance for the E-field along the short axis of the particles (transverse to the particle). Thus, there appears to be a clear tendency of preferred orientation of the long axis of the smaller bi-pyramidal AuNPs (in particular AuNP-B33 and AuNP-B43) in the plane parallel to the two glass surfaces (i.e. for the red-shifted resonance). The bipyramids with smaller aspect ratio are more oriented than the one with larger aspect ratio as shown in figure 8. Moreover, from the measurements it appears that the anisotropy is more important in the bulk than near the surfaces of the materials. From these observations we can anticipate that the orientation is due to forces and solvent flux during the matrix shrinkage and evaporation process. The smaller particles are more mobile than the bigger ones and tend to orientate faster. The short kinetics of the shrinkage/evaporation process allows the smaller particles to fully orientate and generate strong anisotropy in the glass, while the bigger one only partially orientate generating smaller anisotropy.

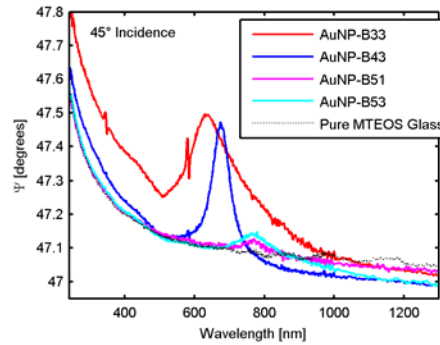


Figure 8. Ellipsometric parameter, ψ , measured with transmission ellipsometry at 45° angle of incidence, for samples AuNP-B33, AuNP-B43, AuNP-B51, AuNP-B53 and pure MTEOS glass. The spikes at approximately 347 and 580 nm are measurement artefacts to be neglected.

For input fluences below approximately 300 J/cm² the optical power limiting measurements at 532 nm laser wavelength shows a relationship between output energy (Q_e) and input fluence (Φ) of

$$Q_e \approx \eta \sqrt{\Phi}, \quad (4)$$

as shown in Figure 9.

η was estimated for each glass material with the linear least square method.[†] As a representative example the raw data and fitted curves for glass materials doped with bipyramidal AuNPs with a plasmon at 640 nm (AuNP-B31 - B33) and the 23 nm diameter spherical AuNP (AuNP-S1 – S4) are shown in Figure 9a and 9b respectively.

Higher concentrations of AuNPs were not followed by a substantial change in the OPL at 532 nm, except for AuNP-S14. This sample had a much higher linear absorption at 532 nm than the other AuNPs. (See the supplementary information.) The linear transmission, for all the materials at 532 nm, is plotted in Figure 10.

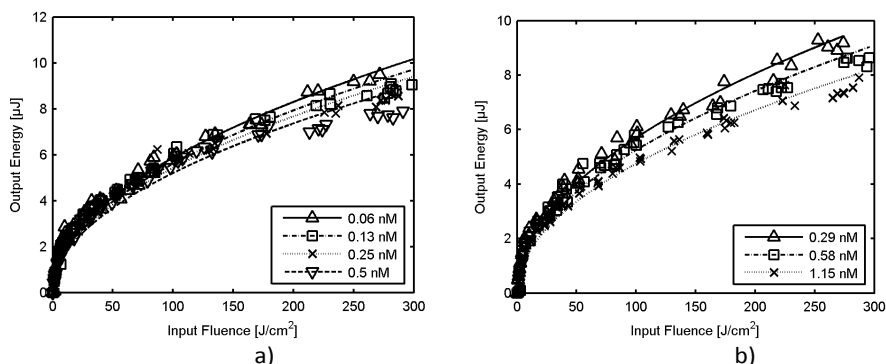


Figure 9. Optical power limiting measurements at 532 nm for glass materials doped with 23 nm diameter AuNPs (AuNP-S1 – AuNP-S4, upper plot) and bipyramidal AuNPs with a plasmon at 640 nm (AuNP-B31 – AuNP-B33, lower plot) The lines are linear least square fits of the output energy to the square root of the input fluence.

In order to investigate the origin of the nonlinear effect, OPL measurements were also made with an integrating sphere. The results for the undoped and doped (AuNP-S2 and AuNP-B42) glass materials are given in Figure 11. The small deviation from linear transmission compared to the optical power limiting measurements without an integrating sphere (Figure 9) shows that scattering is the main mechanism for the observed optical limiting effect in these solids as it is for dispersions.^{28,29}

Previously reported results have shown that the OPL effect, for AuNPs dispersions, decreases with increasing wavelength.²⁸ For the AuNP materials presented here, the optical power limiting measurements at 600 nm laser wavelength showed a linear relationship between input fluence (Φ) and output energy (Q_e) of $Q_e \approx \alpha \Phi$. In other words, no optical power limiting was observed at 600 nm for the AuNP nanocomposites at the input fluences tested. As a representative example, the raw data and fitted lines for AuNP-B31 – AuNP-B33 is shown in Figure 12.

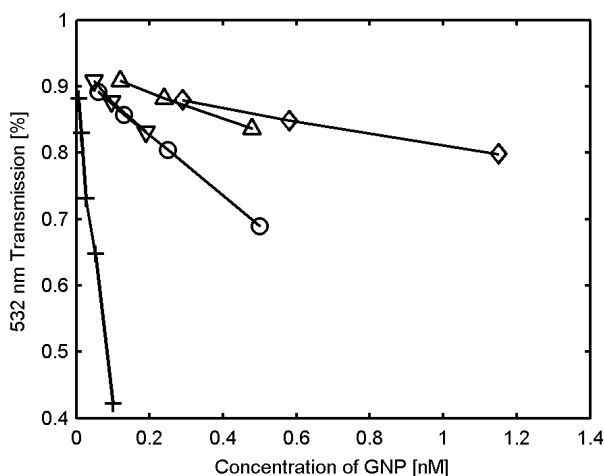


Figure 10. Linear transmission @ 532 nm; AuNP-S1 – AuNP-S4 (o), AuNP-S10 – AuNP-S14 (+), AuNP-B31 – AuNP-B33 (◊), AuNP-B41 – AuNP-B43 (Δ), AuNP-B51 – AuNP-B53 (▽).

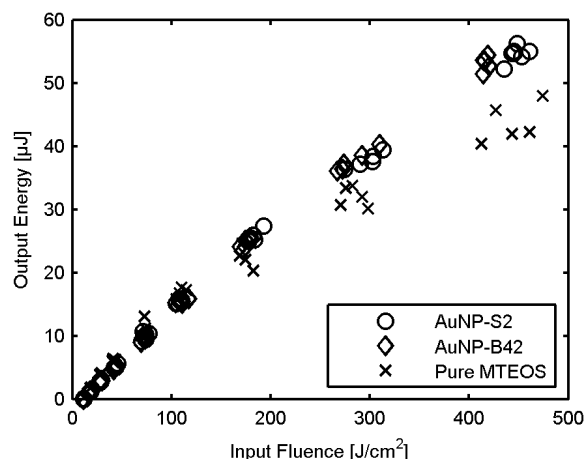


Figure 11. OPL measurements made with an integrating sphere on AuNP-S2, AuNP-B42 and a pure MTEOS glass.

Contrary to what is reported for AuNPs dispersions the size and geometry of the AuNPs in silica does not seem to play a significant role for the OPL effect.^{16,18-21,31} The sizes of the samples presented here ranged from approximately 26 to 45 nm in diameter for the spheres and 36 to 78 nm in length for the bipyramids (16 to 28 nm transversal).

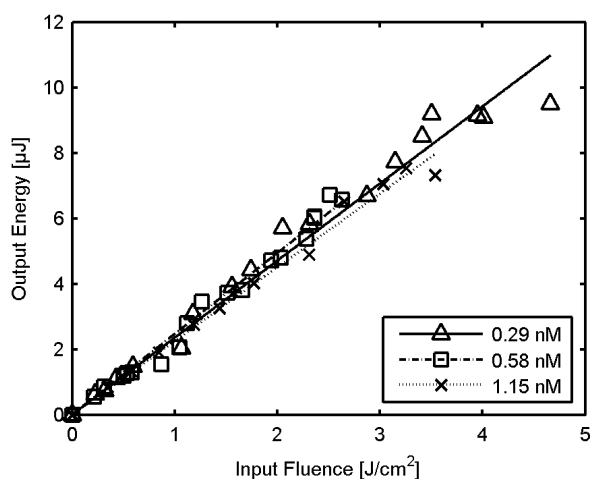


Figure 12. Optical power limiting measurements at 600 nm for AuNP-B31 – AuNP-B33. The lines are linear least square fits of the output energy to the square root of the input fluence.

Conclusions

Several series of MTEOS glasses doped with spherical or bipyramidal gold nanoparticles of varying sizes and concentrations have been prepared using an original silicon polymer for controlling the interface, cut and polished to high optical quality. The shorter bipyramidal AuNPs have a clear preferred orientation in the MTEOS matrix, i.e. their long axis were oriented parallel to the glass surface, but with a random orientation within this plane. Uv-vis spectra showed no redshifts from an increase in AuNP concentration. Thus, there is no or very small LSPR coupling effects in the glasses.

The glass materials showed good optical limiting at 532 nm, which did not depend critically on size or geometry of the AuNPs. Neither did the orientation of the bipyramids affect the OPL. The dominant mechanism behind the OPL response in these solids is scattering. At longer wavelengths, 600 nm, no OPL effect was observed. Further work are in progress to couple in the same matrix both these plasmonic nanostructures and nonlinear chromophores to enhance their optical properties. This approach can easily be extended to other type of metal (Silver...) and metallic nanostructures (rods, cubes, stars..).

References

- 1 N. Li, P. Zhao, and D. Astruc, *Angew. Chem. Inter. Ed.*, 2014, 53 (7), 1756.
- 2 R. Sardar, A. M. Funston, P. Mulvaney, and R. W. Murray, *Langmuir*, 2009, 25 (24), 13840.
- 3 J. E. Millstone, S. J. Hurst, G. S. Métraux, J. I. Cutler, and C. A. Mirkin, *Small*, 2009, 5(6), 646.
- 4 E. W. Malachosky, and P. Guyot-Sionnest, *J. Phys. Chem. C*, 2014, 53 (7), 1756.
- 5 L. Zhang, K. Xia, Z. Lu, G. Li, J. Chen, d. y, S. Li, F. Zhou, and N. He, *Chem. Mater.*, 2014, 118 (12), 6405.
- 6 J. R. G. Navarro, F. Lerouge, G. Micouin, C. Ceperaga, A. Favier, M. T. Charreyre, N. P. Blanchard, J. Lerme, F. Chaput, M. Focsan, K. Kamada, P. L. Baldeck, and S. Parola, *Nanoscale*, 2014, 6, 5138.
- 7 F. Lux, F. Lerouge, J. Bosson, G. Lemerrier, C. Andraud, G. Vitrant, P. L. Baldeck, F. Chassagneux, and S. Parola, *Nanotechnology*, 2009, 20 (35), 355603.
- 8 S. Zaiba, F. Lerouge, A.-M. Gabudean, M. Focsan, J. Lermé, T. Gallavardin, O. Maury, C. Andraud, S. Parola, and P. L. Baldeck, *Nano Lett.*, 2011, 11 (5), 2043.
- 9 J. R. Navarro, D. Manchon, F. Lerouge, E. Cottancin, J. Lermé, C. Bonnet, F. Chaput, A. Mosset, M. Pellarin, and S. Parola, *Nanotechnology*, 2012, 23 (14), 145707.
- 10 J. R. Navarro, D. Manchon, F. Lerouge, N. P. Blanchard, S. Marotte, Y. Leverrier, J. Marvel, F. Chaput, G. Micouin, A.-M. Gabudean, A. Mosset, E. Cottencin, P.L. Baldeck, K. Kamada, and S. Parola, *Nanotechnology*, 2012, 23 (46), 465602.
- 11 J. R. Navarro, A. Liotta, A.-C. Faure, F. Lerouge, F. Chaput, G. Micouin, P. L. Baldeck, and S. Parola, *Langmuir*, 2013, 29 (34), 10915.
- 12 J. R. Navarro, F. Lerouge, C. Ceperaga, G. Micouin, A. Favier, D. Chateau, M.-T. Charreyre, P.-H. Lanoe, C. Monnereau, F. Chaput, S. Marotte, Y. Leverrier, J. Marvel, K. Kamada, C. Andraud, P. L. Baldeck, and S. Parola, *Biomaterials*, 2013, 34 (33), 8344.
- 13 J. Zhang and L. Zhang. *Advances in Optics and Photonics*, 2012, 4 (2), 157.
- 14 D. Chateau, PhD thesis, 2013, University of Lyon, Ecole Normale Supérieure de Lyon, France.
- 15 D. Chateau, A. Liotta, F. Vadcard, J. Navarro, F. Lerouge, F. Chaput, J. Lermé, and S. Parola, Submitted for publication, 2014.
- 16 J. Wang and W. J. Blau, *J. Opt. A: Pure Appl. Opt.*, 2009, 11 (2), 024001.
- 17 G. Wang and W. Sun, *J. Phys. Chem. B*, 2006, 110 (42), 20901.
- 18 L. François, M. Mostafavi, J. Belloni, J.-F. Delouis, J. Delaire, and P. Feneyrou, *J. Phys. Chem. B*, 2000, 104 (26), 6133.
- 19 O. Sánchez-Dena, P. Mota-Santiago, L. Tamayo-Rivera, E. Garcá-Ramrez, A. Crespo-Sosa, A. Oliver, and J.-A. Reyes-Esqueda, *Optical Materials Express*, 2014, 4 (1), 92.
- 20 Y. Gao, Q. Chang, H. Ye, W. Jiao, Y. Li, Y. Wang, Y. Song, and D. Zhu, *J. Chem. Phys.*, 2007, 336 (2), 99.
- 21 R. West, Y. Wang, and T. Goodson, *J. Phys. Chem. B*, 2003, 107 (15), 3419.
- 22 S. Qu, Y. Song, C. Du, Y. Wang, Y. Gao, S. Liu, Y. Li, and D. Zhu, *Optics communications*, 2001, 196 (1), 317.
- 23 G. Piredda, D. D. Smith, B. Wendling, and R. W. Boyd, *JOSA B*, 2008, 25 (6), 945.
- 24 R. Philip, P. Chantharasupawong, H. Qian, R. Jin, and J. Thomas, *Nano Lett.*, 2012, 12 (9), 4661.
- 25 S. Qu, Y. Gao, X. Jiang, H. Zeng, Y. Song, J. Qiu, C. Zhu, and K. Hirao, *Optics communications*, 2003, 224 (4), 321.
- 26 V. Amendola, D. Dini, S. Polizzi, J. Shen, K. M. Kadish, M. J. Calvete, M. Hanack, and M. Meneghetti, *J. Phys. Chem. C*, 2009, 113 (20), 8688.
- 27 S. Dengler, O. Muller, G. Straube, G. Ritt, and B. Eberle, *Proceedings of SPIE*, 2012, 8545.
- 28 L. François, M. Mostafavi, J. Belloni, and J. A. Delaire, *Phys. Chem. Chem. Phys.*, 2001, 3 (22), 4965.
- 29 R. Ganeev, A. Rysanyansky, S. R. Kamalov, M. Kodirov, and T. Usmanov, *J. Phys. D: Appl. Phys.*, 2001, 34 (11), 1602.
- 30 R. Philip, G. R. Kumar, N. Sandhyarani, and T. Pradeep, *Phys. Rev. B*, 2000, 62 (19), 13160.
- 31 B. Eberle, S. Dengler, G. Ritt, and O. Muller. *SPIE Newsroom*, December 2012.
- 32 D. Chateau, F. Chaput, C. Lopes, M. Lindgren, C. Brännlund, J. Öhgren, N. Djourellov, P. Nedelec, C. Desroches, B. Eliasson, T. Kindahl, F. Lerouge, C. Andraud, and S. Parola, *ACS App. Mater. Interfaces*, 2012, 4 (5), 2369.
- 33 R. Zieba, C. Desroches, F. Chaput, M. Carlsson, B. Eliasson, C. Lopes, M. Lindgren, and S. Parola, *Adv. Funct. Mater.*, 2009, 19 (2), 235.
- 34 D. Chateau, Q. Bellier, F. Chaput, K. Kamada, P. Feneyrou, G. Berginc, O. Maury, C. Andraud, and S. Parola, *J. Mat. Chem. C*, 2014, 2, 5105.
- 35 C.-K. Tsung, W. B. Hong, Q. H. Shi, X. S. Kou, M. H. Yeung, J. F. Wang, and G. D. Stucky, *Adv. Func. Mater.*, 2006, 16 (17), 2225.